Supplementary Online Material for

Seismic evidence for a chemically distinct thermochemical reservoir in Earth's deep mantle beneath Hawaii

Authors: Chunpeng Zhao[1], Edward J. Garnero[1,*], Allen K. McNamara[1], Nicholas Schmerr[2], and Richard W. Carlson[3]

Affiliations:

[1]School of Earth and Space Exploration, Arizona State University, Tempe, Arizona 85287-6004, USA.

[2]NASA Goddard Space Flight Center, Planetary Geodynamics Laboratory, Greenbelt, MD 20771, USA.

[3]Department of Terrestrial Magnetism, Carnegie Institution of Washington, 5241 Broad Branch Road, NW, Washington, DC 20015-1305, USA

*Correspondence to: garnero@asu.edu

Supplementary Discussions

Over a dozen high-resolution seismic analyses of detected either sharp lateral boundaries in the lowermost mantle, or strong heterogeneous structures with abrupt transition to the surrounding mantle. Table S1 lists studies that are plotted as thick black lines in Figure S1 on five different shear velocity models and their lateral gradient maps. As seen in Figure S1, the general LLSVP properties are similar from model to model, but the details differ (including tomographically predicted LLSVP height, not shown). Other models that are derivative of collections of models, such as averaging past models (Becker and Boschi 2002) or cluster analysis of models (Lekic et al 2012) also give LLSVP shapes similar to this, especially in our study area. Our results depend on the waveform broadening (misfits) observations, and the patterns do not depend on specifics of any particular tomographic model.

Earthquake information for the high quality data of this study is given in Table S2, with epicenters, stations, and ray paths presented in Figure S3. The lowest parts of ray paths are plotted, showing a dense sampling of the deepest mantle beneath the Hawaiian hotspot.

The misfit measurement in this study measures relative waveform broadening (Figure 3d of the main text), and along with travel time anomalies (Figure S4), are central to detection of the abrupt transition of LLSVP material to surrounding mantle.

Waveform misfits and travel time delays relative to PREM predictions are plotted relative to the S-wave bottoming depth above the CMB for all data in Figure 4 of the main text. We have fairly dense sampling up to 900 km above the CMB with sampling density decreasing above that. The overall trend of the misfits and times are emphasized by the mean values (colored symbols in Figure 4 of the main text) plotted every 30 km in depth. One standard deviation is also plotted (horizontal lines). Waveform misfits increase below 200 km due to *ScS* entering the time window of the *S* wave: *S* and *ScS* become asymptotic to each other, and our *S* windowing scheme erroneously includes some *ScS* energy for delayed *S* waves. Thus, measurements in this study are most robust for *S* waves bottoming between ~ 200-900 km above the CMB. Strong variability is seen in the misfit and time plots at any given depth in Figure 4, most plausibly caused by lateral variations of the sampled mantle structure. Interesting variations with depth are also present: increased waveform misfits near 600 km above the CMB correspond to an onset in increasing travel time delays (see the averages of misfits and times in Figure 4c), although the exact nature of this increasing trend depends upon the reference model. Figure S9 demonstrates this latter point by comparing the travel time anomalies relative to the M1 model (Ritsema et al., 1997), which has a reduced shear wave velocity gradient in the lowest ~200 km of the mantle.

Systematics of the lateral distance of ray path bottoming locations from the cross-section of interest in this study is illustrated in Figure S5. Most rays do not bottom far enough away from the cross-section to greatly affect the depth of the cross-section piercing location.

Fig. S11 (Supplementary Material) provides information on travel times, ray sampling density, and standard deviation of travel times and misfits on the main cross-section investigated in this study. Fig. S12 (Supplementary Material) shows the misfits projected to the cross-section on top of lateral gradients estimated from the tomographic model TBXW (Grand, 2002). Fig. S13 compares broadening for S waves and SS waves at similar stations, and shows how the S waves are disproportionately broadened, arguing for a deep mantle source over the structure beneath stations. Fig. S14 shows misfits projected to the surface, and compares it to velocity structure near the surface. The inconsistency of misfit comparisons to mantle structure suggests near surface structure is not the source of the broadening. This also infers station structure would not conspire to make the consistent pattern of misfits with deep mantle LLSVP structure. Fig S15 shows synthetic experiments with deep mantle attenuation, and Fig. S16 relates broadening (misfits) to differential t* operators.

Additional References

Gu, Y. J., Dziewonski, A. M., Su, W., Ekström, G., 2001. Models of the mantle shear velocity and discontinuities in the pattern of lateral heterogeneities. J. Geophys. Res. 106, 11169-11,199, doi:10.1029/2001JB000340.

He, Y., Wen, L., Zheng, T., 2006. Geographic boundary and shear wave velocity structure of the "Pacific anomaly" near the core–mantle boundary beneath western Pacific. Earth Planet. Sci. Lett. 244, 302-314, doi:10.1016/j.epsl.2006.02.007.

Ni, S., Helmberger, D. V., 2003a. Further constraints on the African superplume structure. Phys. Earth Planet. Inter. 140, 243-251, doi:10.1016/j.pepi.2003.07.011.

Ni, S., Helmberger, D. V., 2003b. Ridge-like lower mantle structure beneath South Africa. J. Geophys. Res. 108, 2094, doi:10.1029/2001JB001545.

Ni, S., Helmberger, D. V., 2003c. Seismological constraints on the South African superplume: could be the oldest distinct structure on Earth. Earth Planet. Sci. Lett. 206, 119-131, doi:10.1016/S0012-821X(02)01072-5.

Ni, S., Helmberger, D. V., Tromp, J., 2005. Three-dimensional structure of the African superplume from waveform modeling. Geophys. J. Int. 161, 283-294, doi:10.1111/j.1365-246X.2005.02508.x.

Porritt, R.W., R.M. Allen, and F.F. Pollitz, 2014. Seismic imaging east of the Rocky Mountains with USArray, Earth Planet. Sci. Lett., 401, 16-25.

Sun, D., and M. S. Miller, 2013. Study of the western edge of the African large low shear velocity province. Geochem.Geophys. Geosyst., 14, 3109–3125.

Sun, D., Helmberger, D. V., Ni, S., Bower, D., 2009. Direct measures of lateral velocity variation in the deep Earth. J. Geophys. Res. 114, 1-18, doi:10.1029/2008JB005873 (2009).

Thorne, M. S., Garnero, E. J., 2004. Inferences on ultralow-velocity zone structure from a global analysis of SPdKS waves. J. Geophys. Res. 109, B08301, doi:10.1029/2004JB003010.

Wang, Y., Wen, L., 2004. Mapping the geometry and geographic distribution of a very low velocity province at the base of the Earth's mantle. J. Geophys. Res. 109, 1-18, doi:10.1029/2003JB002674.

Table S1. Past seismic studies that image Large Low Shear Velocity Province (LLSVP) margins. The Location Number corresponds to Figure 1b and 1c in the main text.

Location Number	Region (*Reference*)	Seismic Phases Used
1	West Pacific (*He et al., 2006*)	*S, ScS*
2	North Pacific (*Luo et al., 2001*)	*PKP*
3	North Pacific (*Bréger and Romanowicz, 1998*)	*S, SKS, SKKS*
4	East Pacific (*Sun et al., 2007*)	*PKP*
5	South Pacific (*To et al., 2005*)	*S, SKS, SKKS*
6	South Pacific (*Ford et al., 2006*)	*S, SKS, SKKS*
7	Middle Pacific (*He and Wen, 2009*)	*S, ScS, SKS, SKKS*
8	South Africa and Atlantic (*Wang and Wen, 2004*)	*S, ScS, SKS, SKKS*
9	South Africa (*Sun et al., 2007*)	*S, ScS, SKS, SKKS*
9	South Africa (*Sun et al., 2009*)	*S, ScS, SKS, SKKS*
10	South Africa (*Ni and Helmberger, 2003a*)	*S, ScS, SKS, SKKS*
10	South Africa (*Ni and Helmberger, 2003b*)	*S, ScS, SKS*
10	South Africa (*Ni and Helmberger, 2003c*)	*S, ScS, SKS, P, PcP*
10	South Africa (*Ni et al., 2005*)	*S, ScS, SKS*
11	West Africa (*Sun and Miller*, 2013)	*S, ScS, SKS, SKKS*

Table S2. Earthquake information (from NEIC) for events used in this study.

Date	Latitude (deg)	Longitude (deg)	Depth (km)	Mag.
07 Aug. 2006	-15.80	-167.79	150	6.8
26 Aug. 2007	-17.46	-174.34	127	6.0
05 Oct. 2007	-25.19	179.46	509	6.0
16 Oct. 2007	-25.77	179.53	509	6.0
15 Jan. 2008	-21.98	-179.54	597	6.0
03 Jul. 2008	-23.37	-179.78	581	6.0
19 Jul. 2008	-17.34	-177.31	391	6.0
22 Oct. 2008	-18.42	-175.36	233	6.0
04 Nov. 2008	-17.14	168.46	206	5.7
08 Nov. 2008	-15.20	-174.20	121	5.4
26 Apr. 2009	-30.35	-178.51	131	6.5

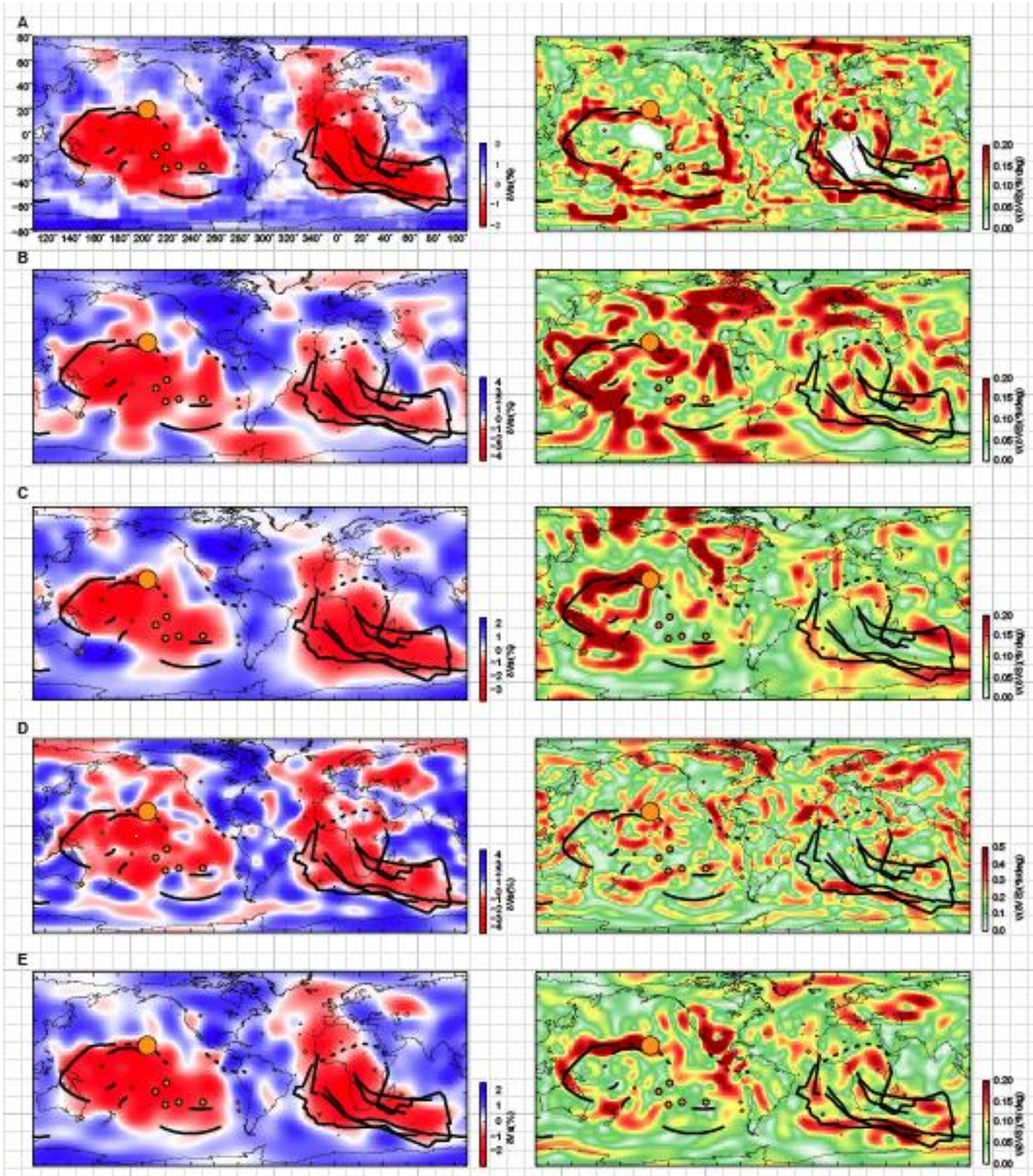

Figure S1. Geographic correlation of hotspots and edges with different tomography models. (a) Grand, 2002; (b) Gu et al. 2001; (c) Masters et al. 2000; (d) Mégnin and Romanowicz, 2000; (e) Ritsema et al. 2011. Left column: hotspot locations (orange circles) are plotted on top of 5 different global tomography shear velocity models at 2750 km depth. Blue and red colors represent higher and lower velocities, respectively.

Hotspot size is scaled to the flux of each hotspot (Sleep, 1990). Lateral shear velocity gradients are shown in the right column (red = strongest gradients). The locations of LLSVP margins found in forward modeling studies are shown in all the panels as thick black lines (the lines are dashed if from travel time analyses). The source studies are indicated in Figure 1 of the main text, and in Table S1.

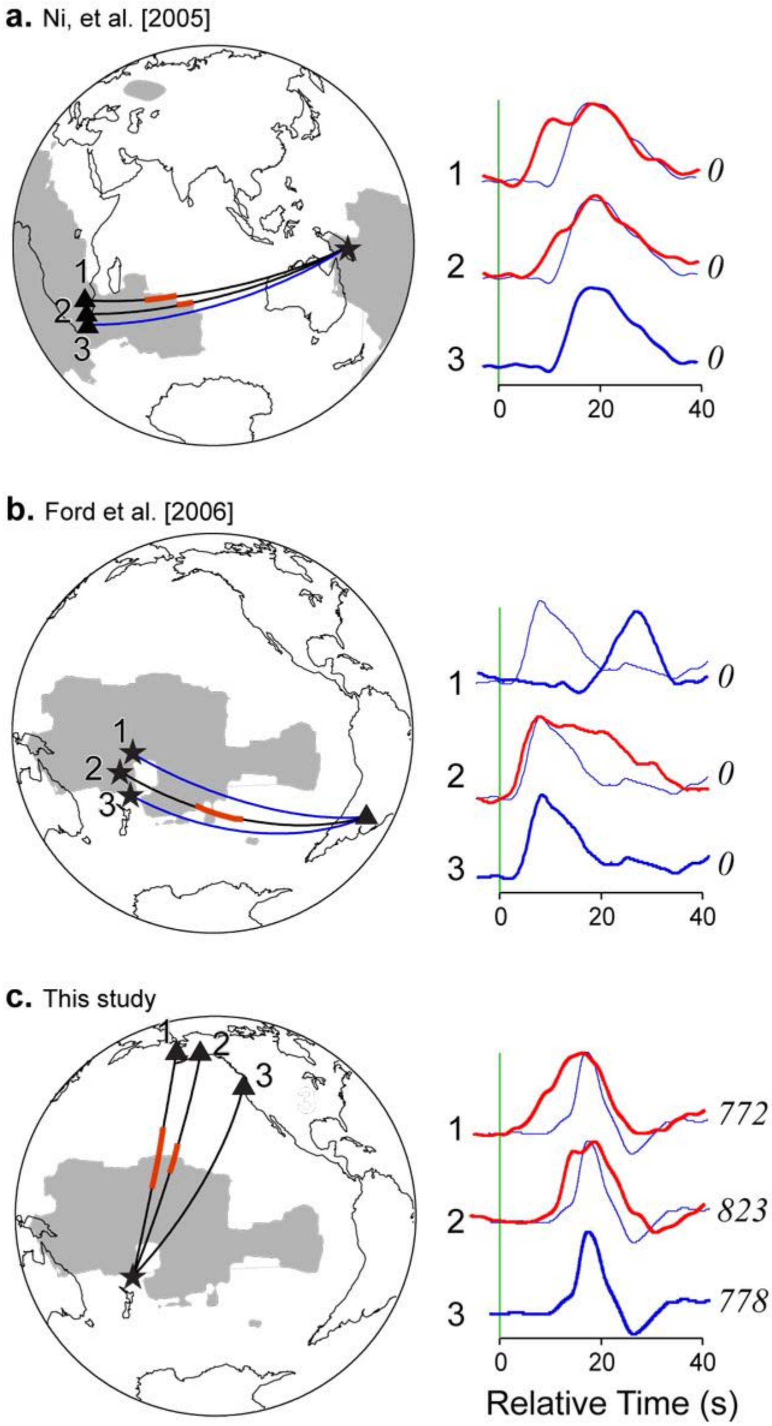

Figure S2. Examples of seismic waveform broadening from S-waves that propagate near LLSVP margins. Globes display earthquakes (stars), receivers (triangles), ray path geometries (black lines; red segments indicate lower mantle part of path for broadened pulses), for the studies of (a) Ni et al. 2005, (b) Ford et al. 2006, and (c) this study. Shaded regions are LLSVPs (all areas with shear velocity < -1.1%, from model TXBW (Grand, 2002)). Corresponding waveforms are numbered according to ray paths in globes. Numbers on the right of waveforms are the bottoming depth of ray paths in km. Panels (a) and (b) have broadened waveforms from propagation nearly tangent to LLSVP margin, at the base of the mantle (thus the waves are diffracted S-waves). Panel (c) shows broadening up off the core-mantle boundary, for paths that are nearly orthogonal to the LLSVP margin.

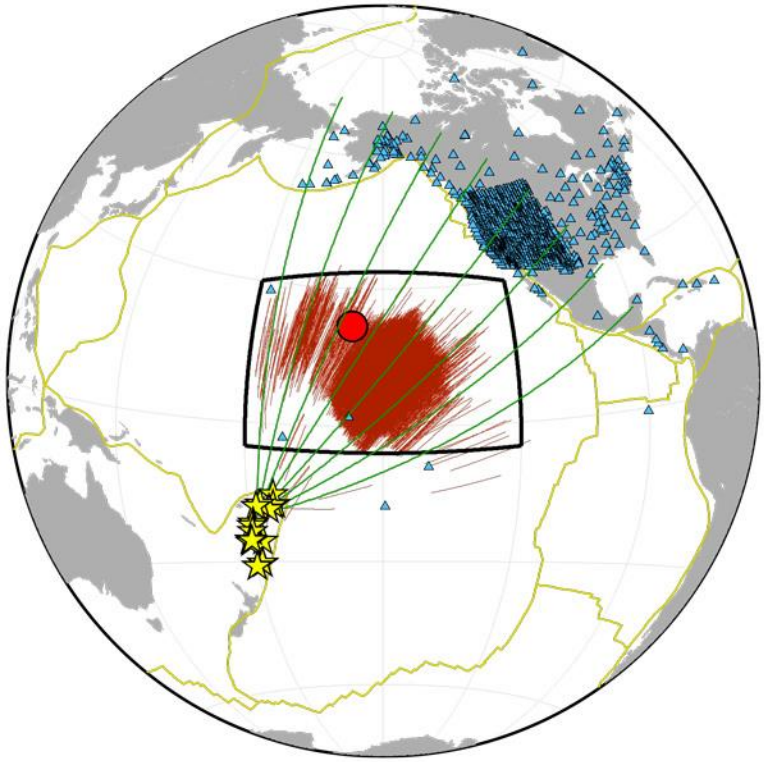

Figure S3. Distribution of our data. Distributions of earthquake sources (yellow-filled black stars), receivers (blue-filled triangles), and the lowermost 50 km segments of all the S-wave raypaths (red line segments) are plotted along with the location of our study region (black box). Large red-filled circle denotes the Hawaiian hotspot. Thick tan lines indicate plate boundaries. Earthquake information is provided in Table S2. Green lines emphasize azimuth from a common source, the dominant geometric factor in distinguishing ray path segments in our study region.

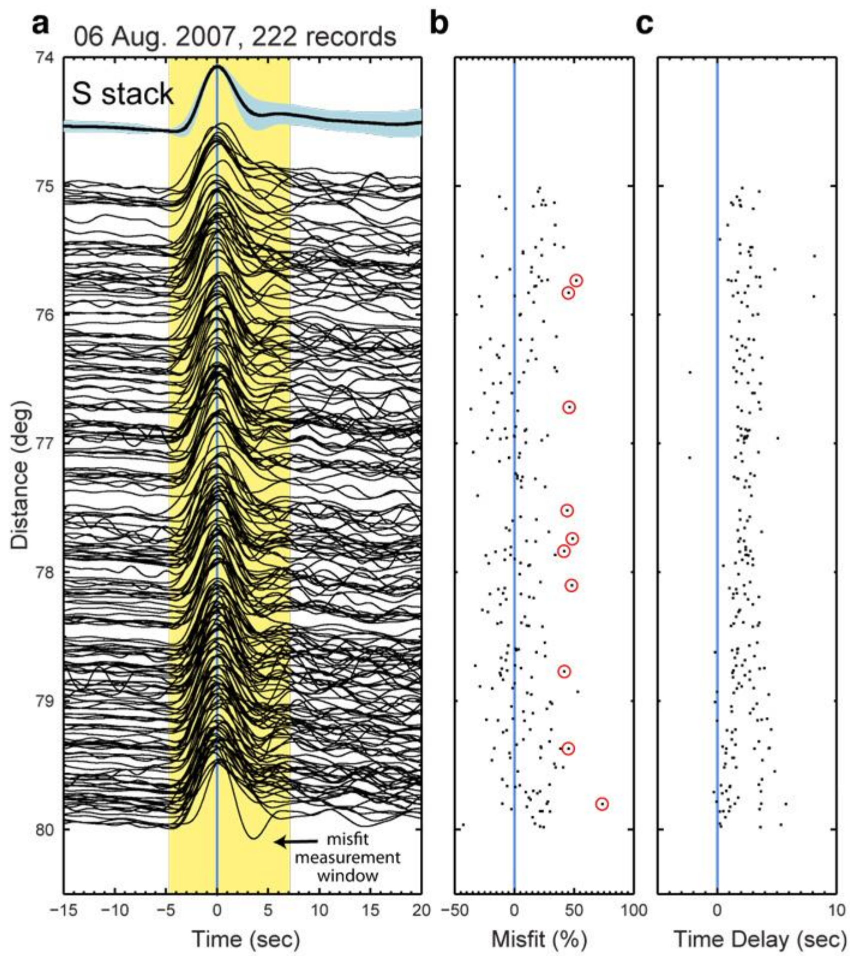

Figure S4. Waveforms, misfits, and travel times for an example earthquake. (a) Example transverse component displacement S-wave recordings from the August 26, 2007 earthquake (left column). The empirical source shape is shown at the top of the distance profile (as in Figure 2 of the main text), along with the standard deviation (light blue shading). Records are aligned according to their maximum cross-correlation with the empirical source, in the 12-second window shown (yellow shaded region). (b) The middle panel displays measured misfits for the data of panel (a) with circles around measurements that correspond to the ten broadened records shown in Figure 2 of the main text. (c) Travel time anomalies are plotted relative to the PREM-predicted *S* wave times. Nearly all of these data display travel time delays associated with the Pacific

LLSVP.

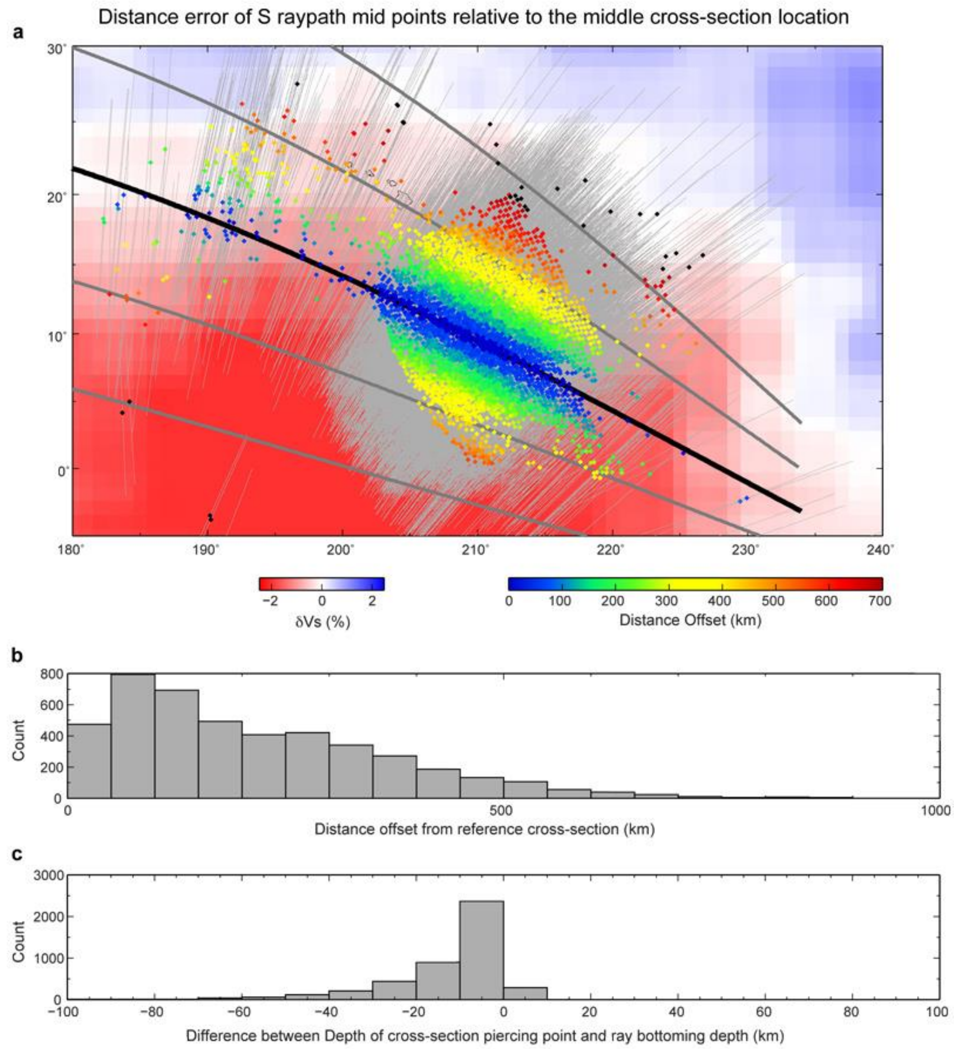

Figure S5. Ray path bottoming location geometry relative to cross-section. (a) Sampling of the NW Pacific is shown with gray lines representing the bottom 50 km of ray path bottoming locations, underlain by the lowermost mantle shear velocity tomography model of TXBW (Grand, 2002). Colored dots represent the turning depth location of raypaths, with color denoting the perpendicular distance between ray path bottoming location and the thick black cross section line, and black dots are for distances greater than 700 km. Thick gray cross-section lines are parallel to black cross-section line, roughly separated in 500 km intervals. (b) Histogram displaying perpendicular horizontal distance between ray path bottoming depths and the black cross section line. Most of the data are within several 100 km of the cross section. (c) Histogram displaying the vertical offset of ray path bottoming depth, and the depth that each ray path intersects the cross-section. Here it is seen that ray paths do not turn at depths remarkably different from cross-section piercing depths.

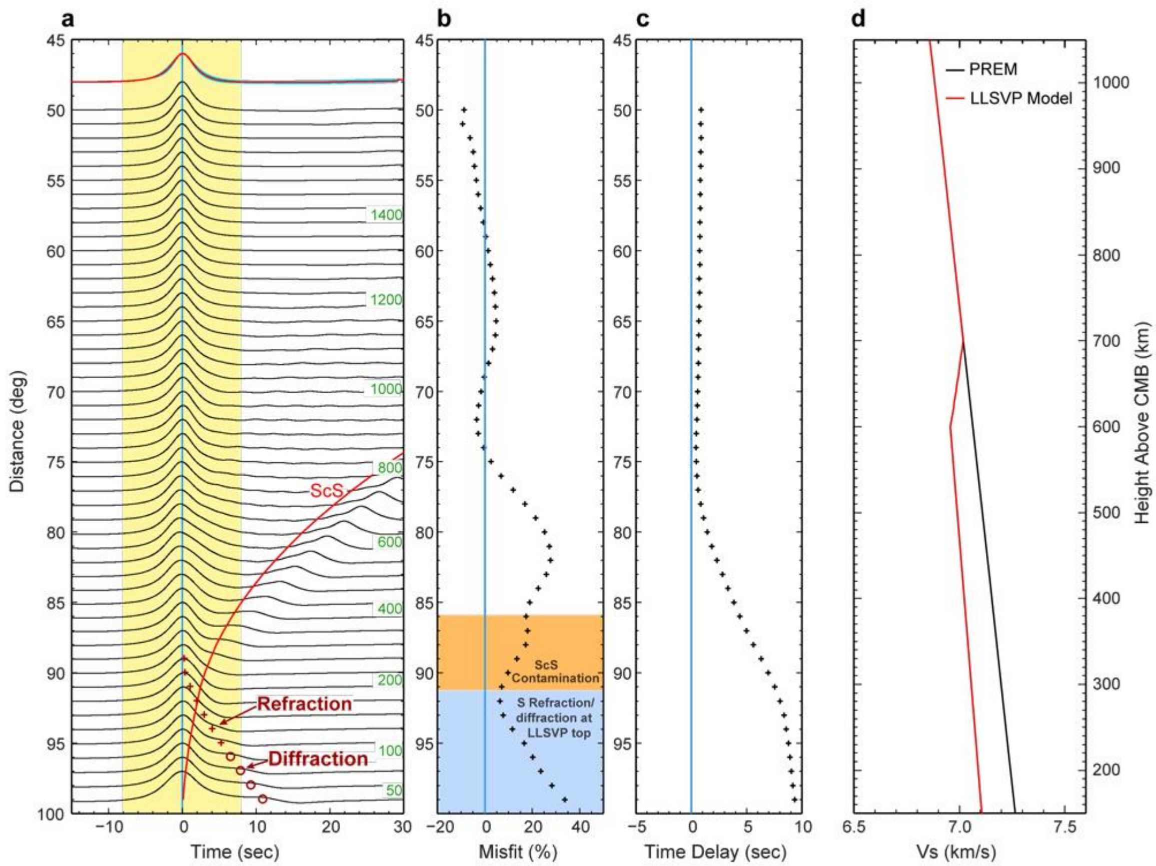

Figure S6. Synthetic seismograms showing misfit effects from other seismic phases. (a) The empirical source stack (red trace at top) is obtained using the same method as we do with data. All displacement synthetic seismograms are aligned on the peak of S wave (blue line). Yellow shaded region denotes the misfit measurement time window. Red curve indicates the PREM predicted arrival time of ScS relative to the S-wave. Red crosses are the arrival time of a phase refracting along the top of the LLSVP low velocity layer, and red circles denote when this phase begins diffracting along the top of the layer. Ray path bottom depth predictions are printed in green on the right side of the panel. (b) Misfit measurements (black crosses) are computed for the synthetic seismograms of panel (a). Distance ranges of ScS contamination to the misfit measurement have orange shading, and distances where contamination occurs from an S-wave refracting or diffracting along the top of the LLSVP (above the LLSVP in the mantle) are plotted in blue. (c) Travel time delays measured for the S-waves of panel (a). (d) The LLSVP model (red) and PREM (black) are plotted with respect to the height above the CMB in kilometers.

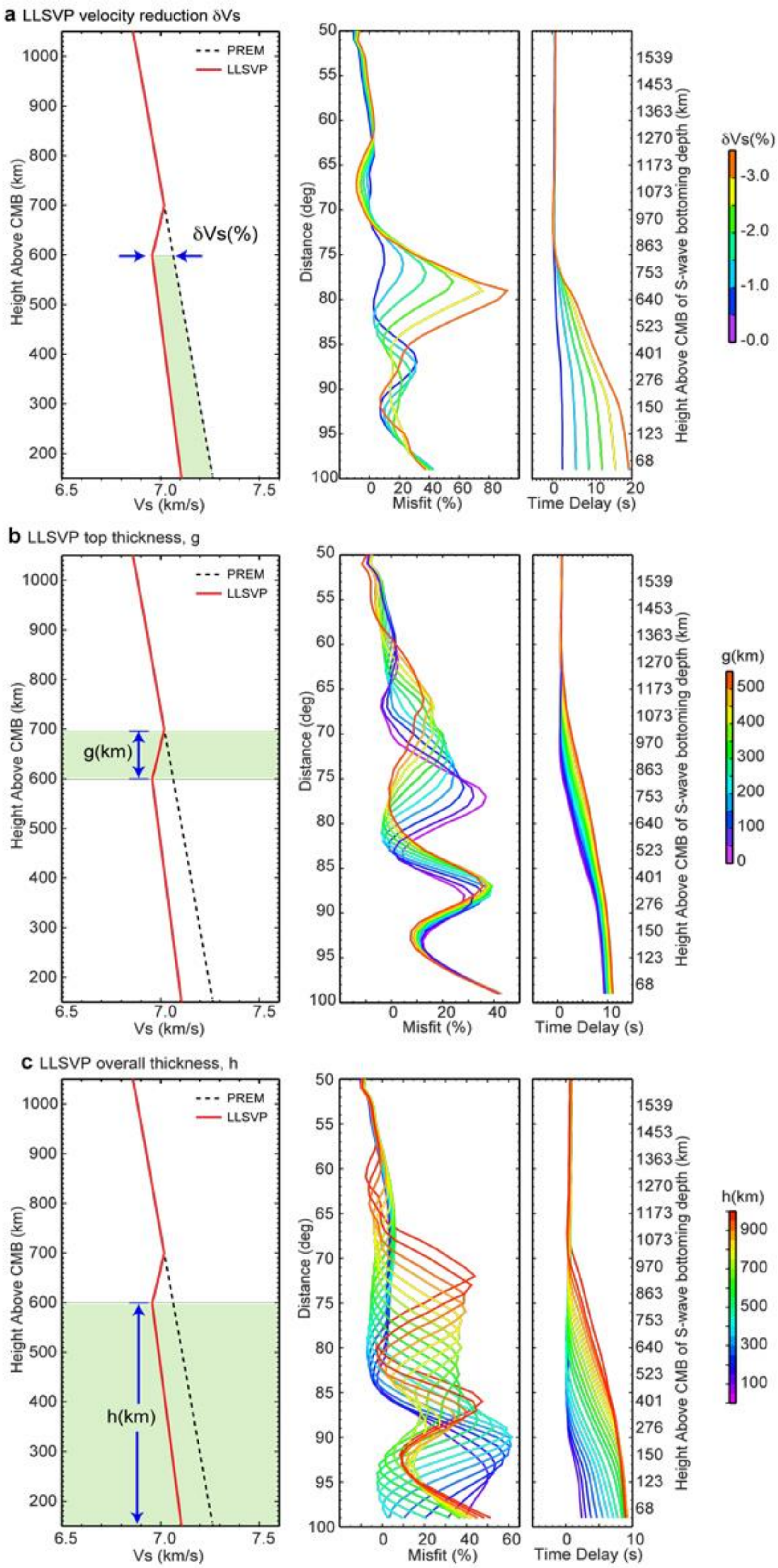
a LLSVP velocity reduction δVs
PREM
LLSVP
δVs(%)
Height Above CMB (km)
Vs (km/s)
Distance (deg)
Misfit (%)
Time Delay (s)
Height Above CMB of S-wave bottoming depth (km)
δVs(%)
b LLSVP top thickness, g
g(km)
c LLSVP overall thickness, h
h(km)

Figure S7. LLSVP Synthetic Tests. Waveform misfits and travel time delays for synthetic models are measured using the same method as we do with data. Each row of this figure corresponds to a specific LLSVP model attribute, with the model (left), the misfit (center), and travel time delay (right) being shown. (a) Shear velocity reduction within the LLSVP (δVs): constant reductions are tested, from 0 to 3.5%. Here the LLSVP is 600 km thick, with a 100 km thick taper zone back to the PREM model. (b) Varying thickness of a gradient zone from normal (PREM) mantle to LLSVP mantle (g) is tested. The LLSVP velocity reduction is fixed at 1.5% for the models shown, and the depth at the top of the linear gradient is at 700 km above the CMB. (c) The thickness of the LLSVP from the CMB up to the base of the gradient zone (h) is tested. A 1.5% LLSVP velocity drop and a 100 km gradient zone at the top are used for these models. While only end-member models are shown, all combinations of parameters where computed (over 1000 models).

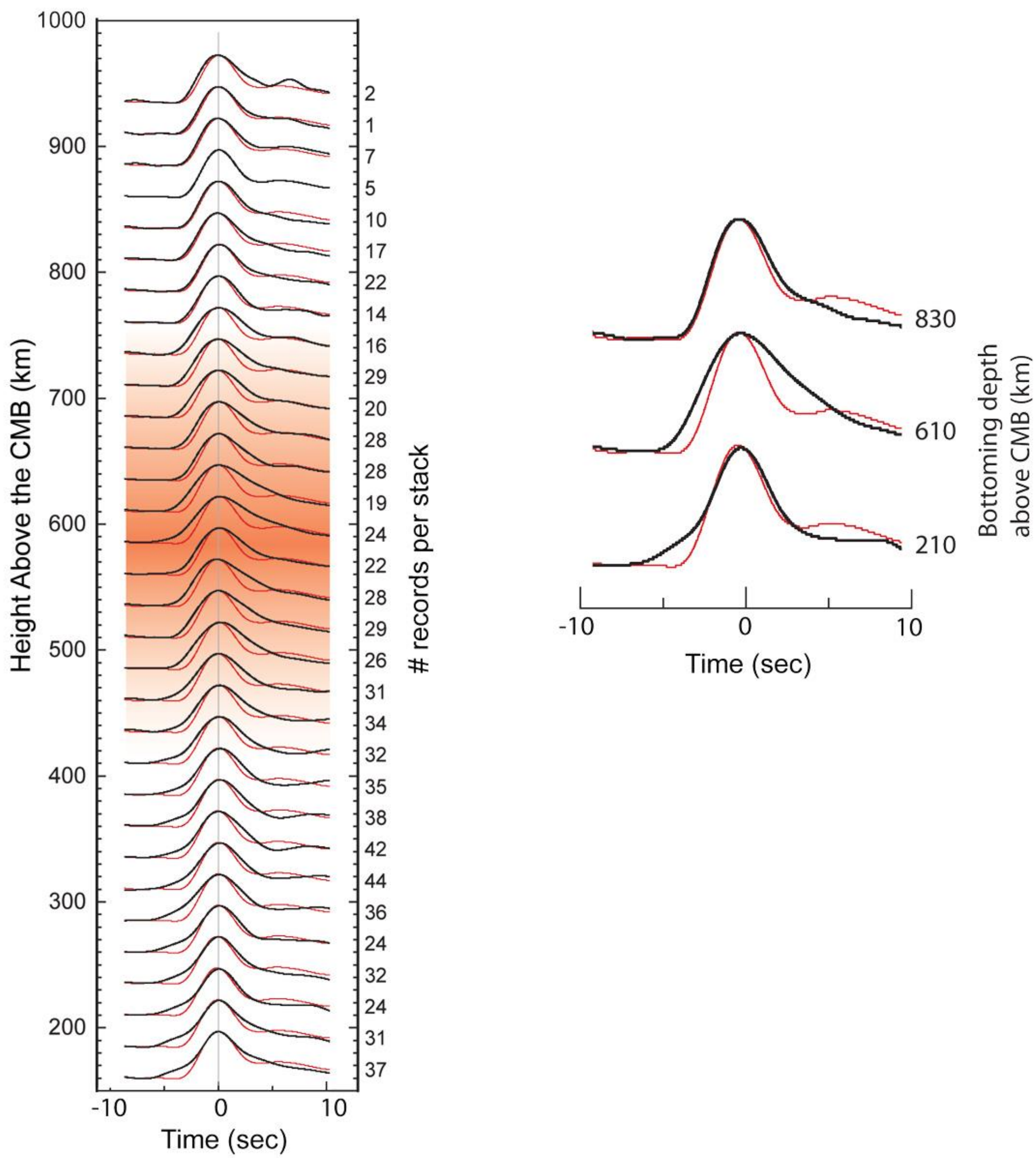

Figure S8. Stacking data for the restricted azimuth sector of Figure 6a. (left) Records are binned in 25 km bottoming depth groupings, and stacked via an iterative cross-correlation algorithm (black traces). The number of traces in each stack is shown to the right of this panel. The stack at 860 km is used as a reference, and plotted in red beneath all stacks, which shows the broadening of the stacked traces in the 400-750 km range, especially near 600 km above the CMB (the orange shading highlights this region). (right) Stacks at

210, 610, and 830 are enlarged to demonstrate the deeper (210) and shallower (830) stacks are similar to the reference, but the stack at 610 is significantly broadened. These stacks are a waveform equivalent of misfit information plotted in Figure 6d of the main text.

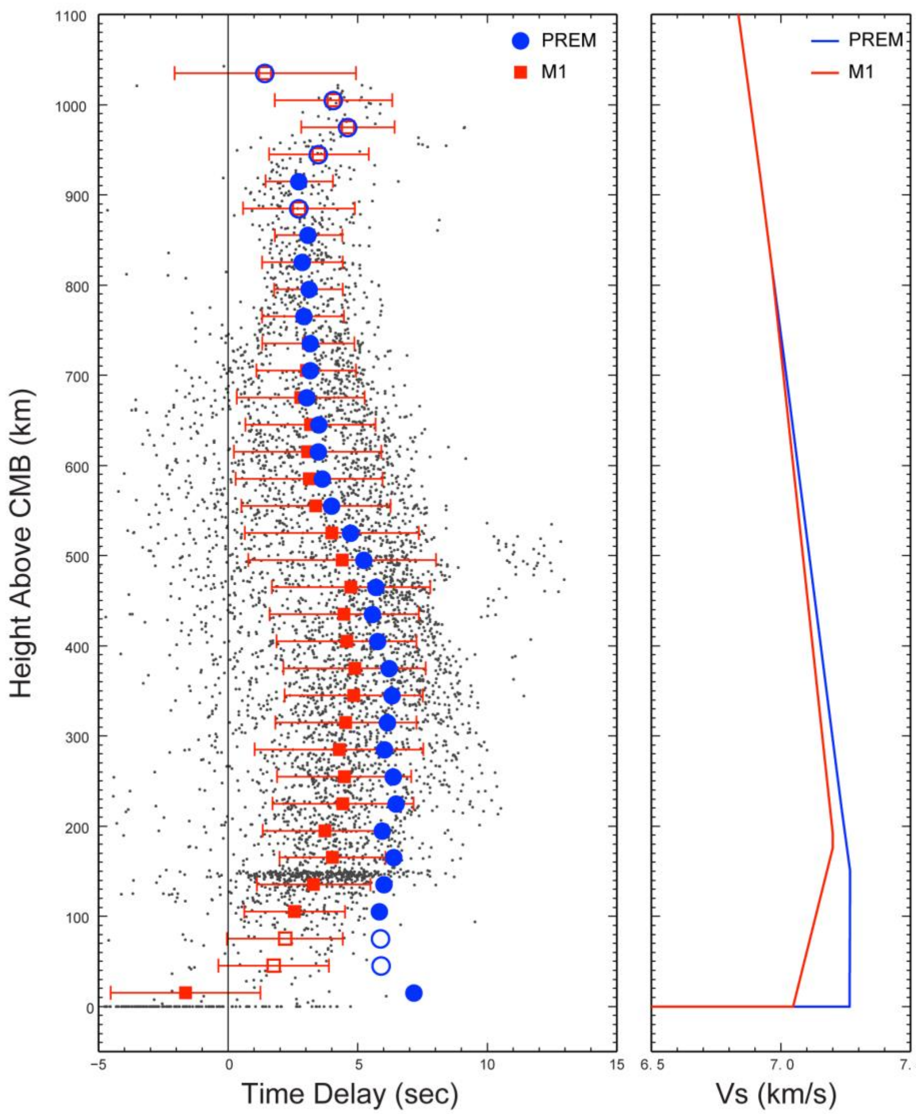

Figure S9. Dependency of travel time delays on 1D reference model. (left) Absolute travel time anomalies of S-waves (gray dots) are shown referenced to predictions of the M1 model (Ritsema et al., 1997). As with Figures 4b and 6e in the main text, times are plotted at bottoming depths computed for the PREM model. Depth-bin averages (red squares for M1, blue circles for PREM) and +/- one standard deviation (horizontal bars) are calculated in 30 km depth intervals. Open symbols correspond to depth bins with fewer than 20 measurements. (right) The M1 (red) and PREM (blue) shear velocity models are shown.

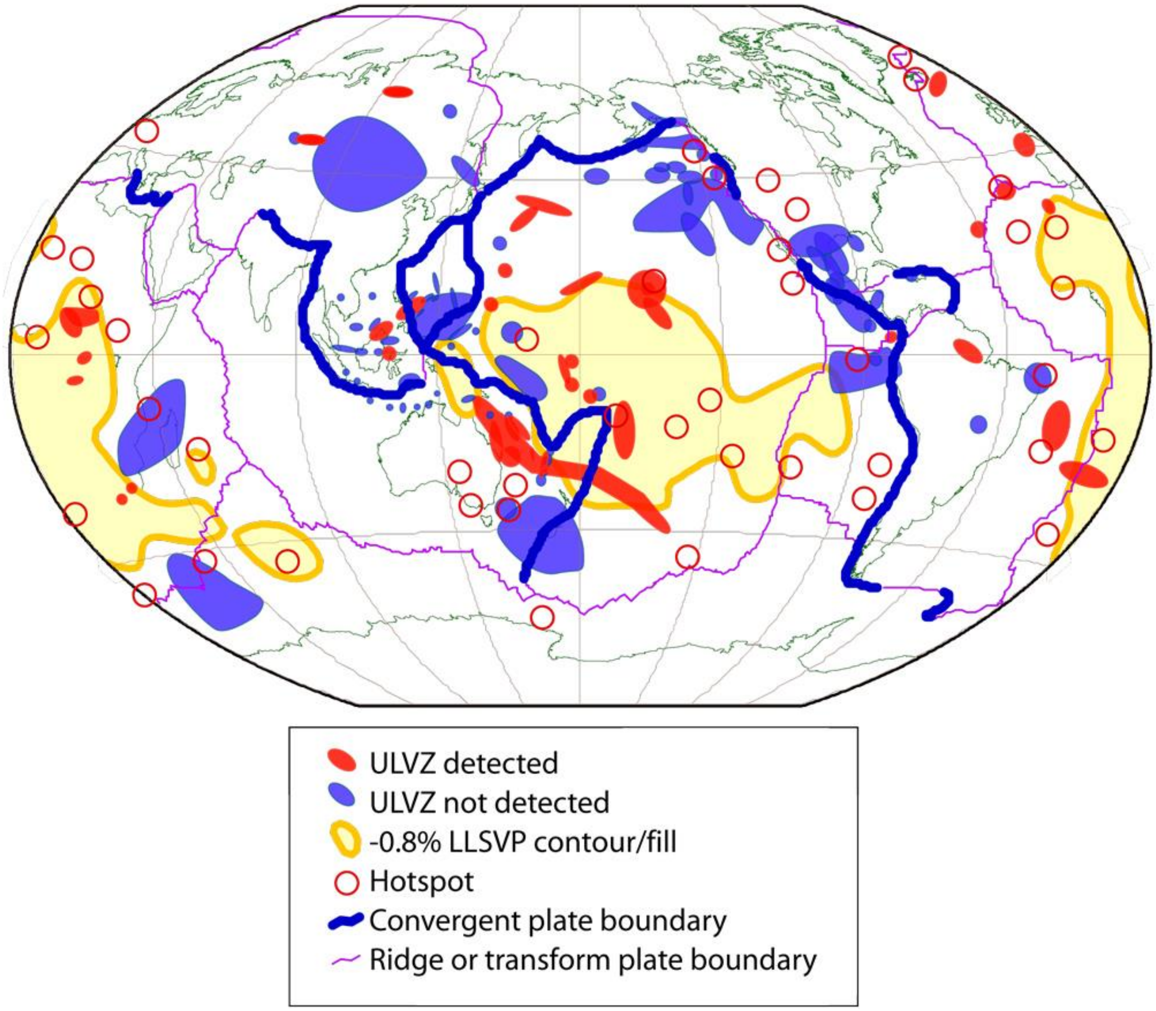

Figure S10. LLSVP in relationship to ULVZs and other phenomena. The CMB is not uniformly sampled in ULVZ studies (McNamara et al., 2010; Thorne and Garnero, 2004). But where it is studied, it appears that ULVZ detection (red spots) is often near LLSVPs (yellow shading), particularly the boundaries. However, many ULVZs are outside LLSVPs. ULVZ non-detections are usually outside LLSVPs, and close to regions beneath present-day subduction zones (see blue lines). Hotspots are commonly near LLSVP boundaries (Thorne et al., 2004), but exceptions exist. ULVZ regions are from McNamara et al. (McNamara, et al., 2010). Hotspots are from Sleep (Montelli et al., 2004).

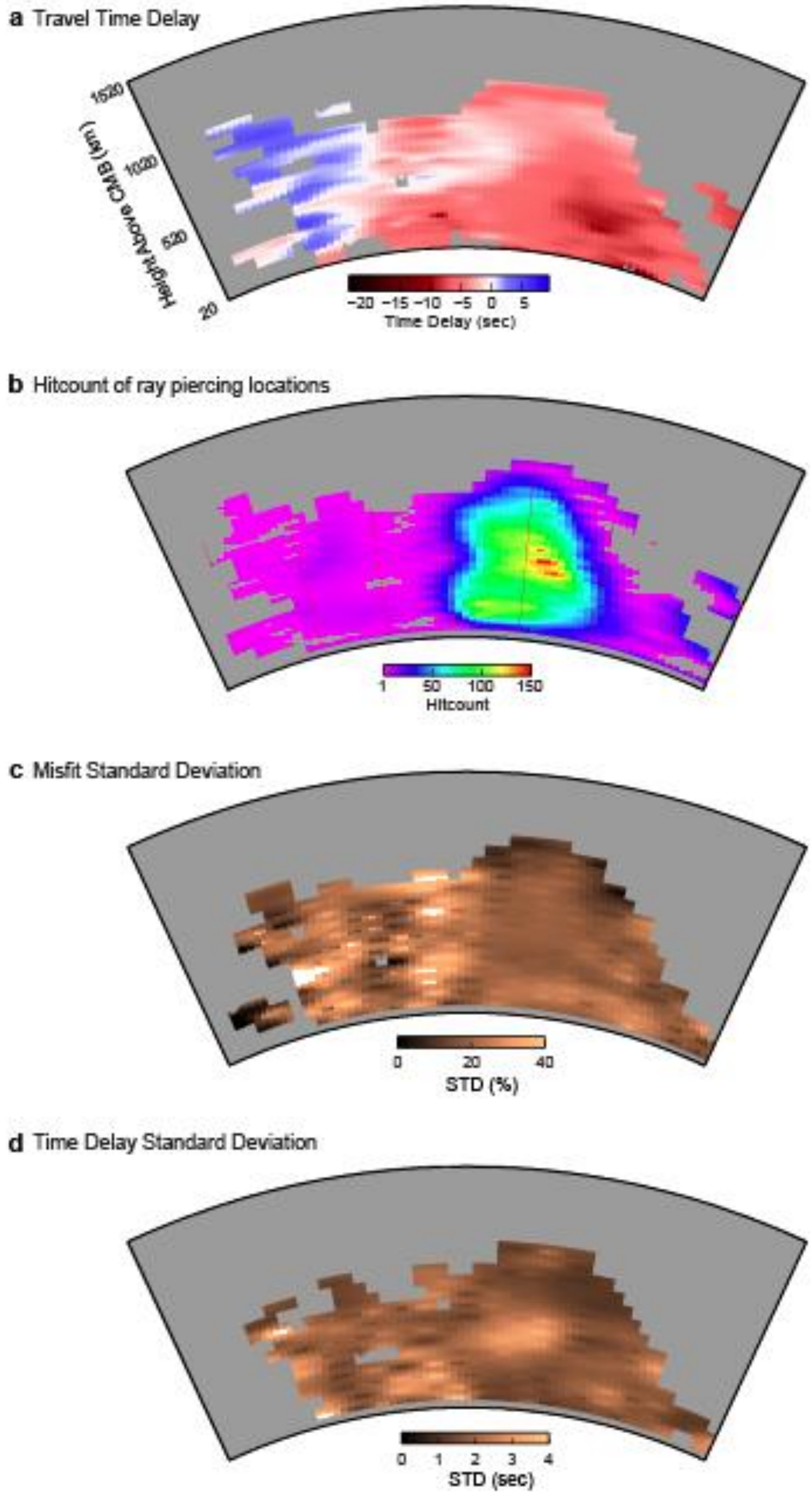

Figure S11. Distribution of data delay times, hitcount, and standard deviation. (a) S-wave travel time delay anomalies (relative to PREM) projected on to the same cross-section used in previous figures. Travel time delays (red regions) mimic the shape of the tomographically derived LLSVP shown in other figures (e.g., Figure 6b of the main text). Gray areas represent no coverage. (b) Number of sampling ray paths on this cross-section. Much of the LLSVP region is well sampled. Regions without wave sampling are shaded gray. (c) Standard deviation of misfits, which shows that for the region with best coverage (the LLSVP region), the misfit measurements do not significantly vary. (d) As in (c) except the standard deviation of travel time anomalies is shown.

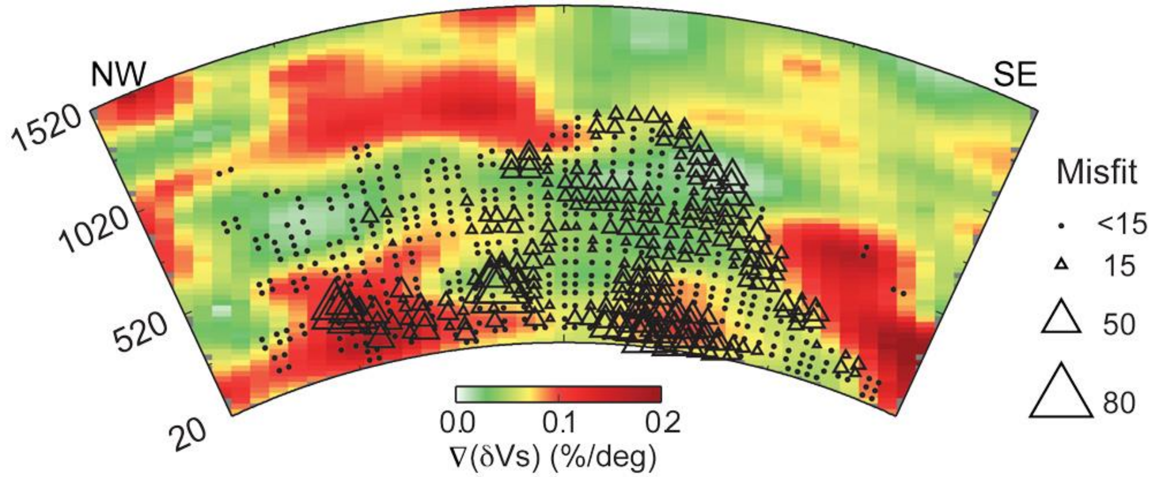

Figure S12. Correlation between waveform misfits and tomography gradients. Waveform misfits are plotted on the NW-to-SE cross-section (as with Figure S11). Here, the background displays lateral gradients in shear velocity heterogeneity in the TXBW model (Grand, 2002). The strongest gradients in TXBW are red, and in the lowest 600 km of the mantle agree well with either the boundary or location of the largest misfits.

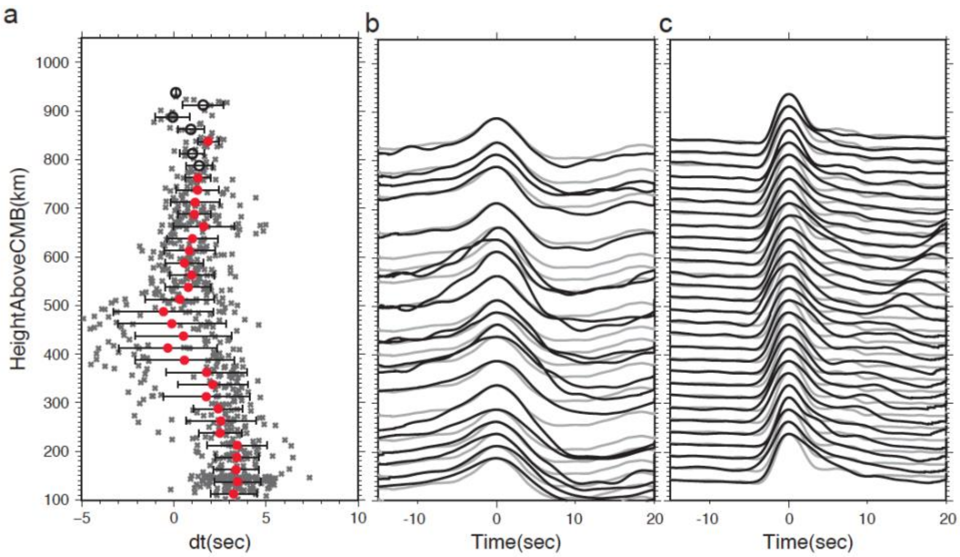

Figure S13. (a) S travel times within the azimuthal bin in Fig. 6 are corrected by TXBW relative to PREM using PREM predicted ray paths. Depth bin average (red dots), and standard deviation (black bars) are plotted on top of tomography model corrected travel times (gray crosses). Some data in the 300-500 km depth range above the CMB differ from the general trend of travel time delays, and may be due to sampling in the northeast of our study region, plausibly just outside the LLSVP in higher velocities. (b) SS waveform bin stacks for the same azimuthal bin as in Fig. 6, and the same records (where possible) from which S waves are studied, are plotted for 25 km bottoming depth bins (thicker black traces) -- here, the bottoming depths correspond to the S waves; SS waves for the same records are grouped similarly. Gray traces are copied from the 3rd bin from the top as a reference to illustrate that the SS depth bin stacks show little or no broadening with depth. (c) S wave depth bin stacks, as done in panel (b). Gray traces are copied from the 4th bin stack from the top as a reference, which shows that the S stacks broaden most strongly between 600-700 km above the CMB (whereas SS waves do not broaden for those bins).

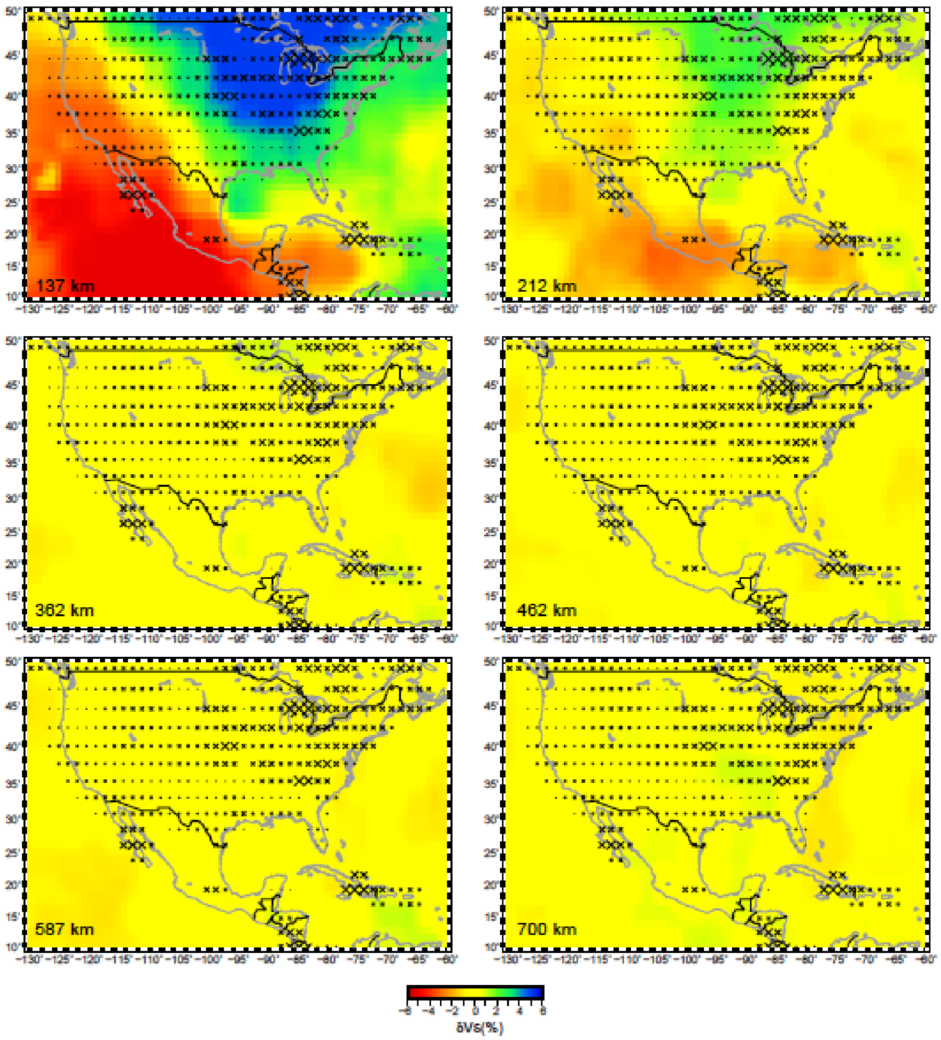

Figure S14a. S misfit measurements have been projected to the locations of the stations, then smoothed onto a 1.5 deg by 1.5 deg grid (black crosses); these are ten overlaid on the TXBW shear velocity model in the upper mantle. Number in the lower left corner stands for the depth of the tomography model perturbations. The strong misfits are not seen in the western US (which corresponds to S-waves bottoming above the LLSVP). In the eastern half of the US, discreet and unconnected patches of broadening are seen. The large misfits appear more spatially correlated to LLSVP edges (e.g., Fig 6).

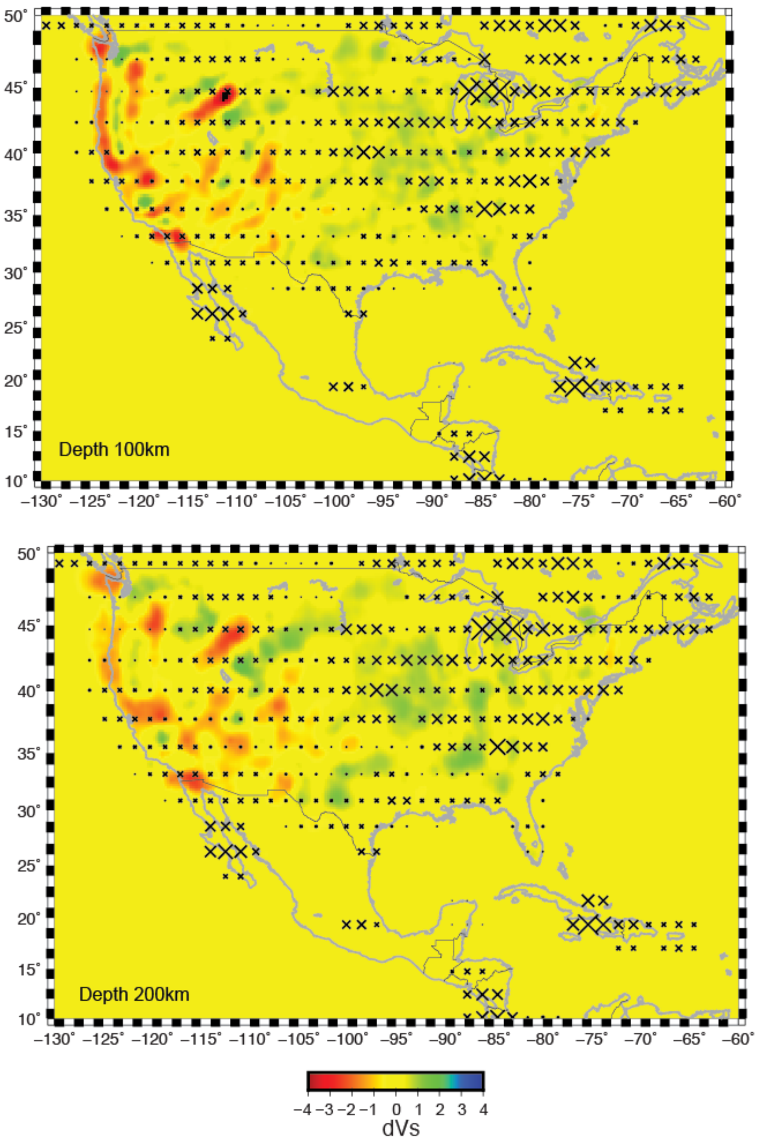

Figure S14b. As in Fig. S14a, except comparisons are made for an upper mantle tomography model of Porritt et al. (2014).

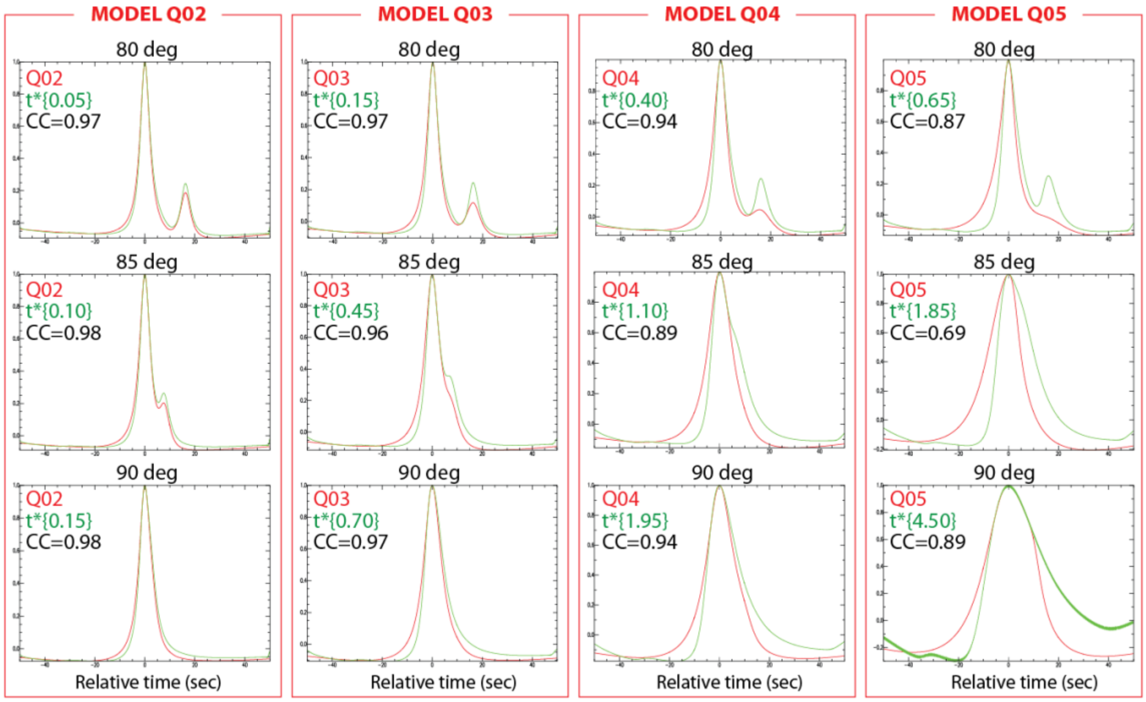

Figure S15. Synthetic tests of low Q (high attenuation) models in the lowest 600 km of the mantle. Synthetics are computed for SH traces using the reflectivity method, and a 500 km deep source. Each row of panels corresponds to different distances: 80 deg (top row), 85 deg (middle row), and 90 deg (bottom row). Each column corresponds to a different lower mantle Q model, where the PREM model is used for the synthetics except the shear Q value is lowered to a constant value in the lowest 600 km of the mantle as follows: Q02=200 (column 1), Q03=100 (column 2), Q04=50 (column 3), Q05=25 (column 4); The PREM value for Q in this depth range is 312. All red traces are synthetics for that corresponding Q model (column) and distance (row). The secondary peak at small distances is ScS, the main peak is direct S. Green traces are a result of convolving PREM traces (with PREM's Q=312) with a differential t* operator that gives a best fit to the particular reduced Q model. Best-fit differential t* values (in seconds) are listed in each panel in the upper left. Differential t* values are smallest for the more shallow diving waves (e.g., 80 deg), and for milder Q drops (e.g., Q02). Cross-correlation coefficients between low Q traces and best-fit green traces are also shown. Traces are plotted with peaks aligned to show that the upswing and downswing portion of pulses increasingly differs for the lowest Q models, which reduces the cross-correlation coefficient.

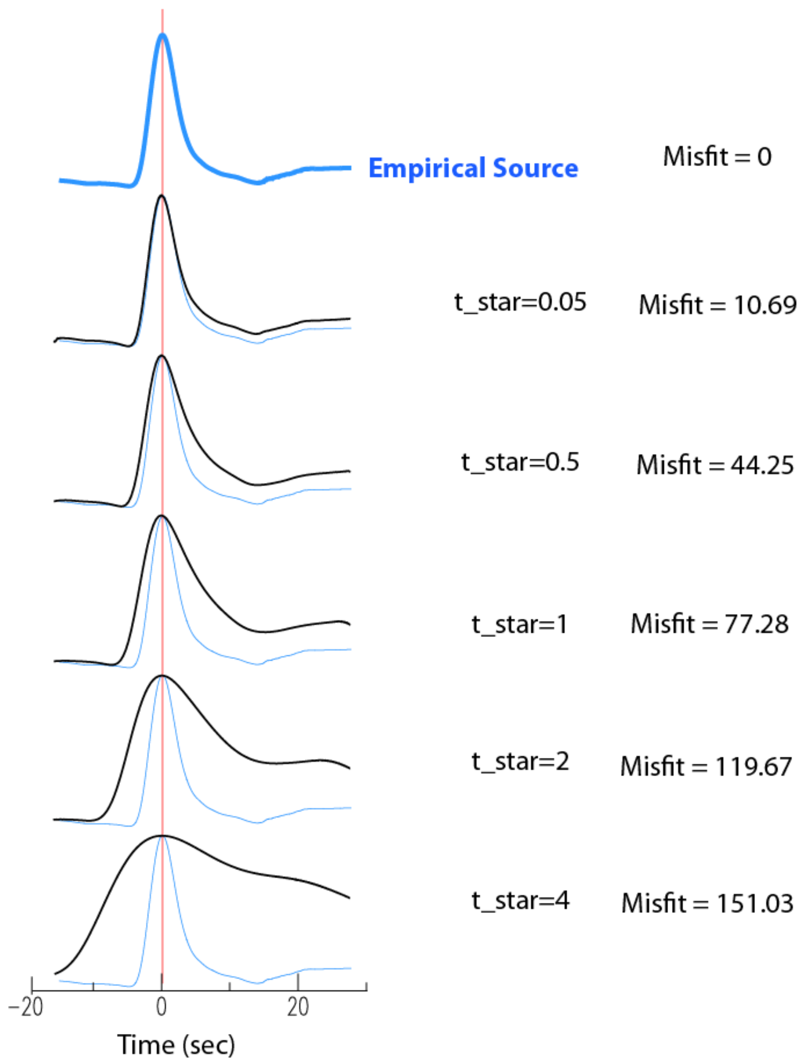

Figure S16. An example empirical source wavelet from one of our events (blue top trace) convolved with a suite of t* ("t_star") values (listed on the right, in seconds), black traces. The empirical source wavelet is reproduced with each black trace, and misfit values (as defined in the main text) are computed, and listed on the right. S